Progress in ion beam figuring of very thin slumped glass plates for lightweight x-ray telescope

M. Civitani, M. Ghigo, J. Holyszko, G. Vecchi, S. Basso, et al.

SPIE.

Progress in ion beam figuring of very thin glass plates for lightweight X-ray telescopes

M. Civitani[1a], M. Ghigo[a], J. Hołyszko[2a], G. Vecchi[a], S. Basso[a], V. Cotroneo[b], C. T. DeRoo[b], E. D. Schwartz[b], P. B. Reid[b]

(a) INAF-Brera Astronomical Observatory, Via E. Bianchi 46, I-23807 Merate (LC), Italy
(b) Harvard-Smithsonian Center for Astrophysics, Cambridge, United States

ABSTRACT

The combination of the hot slumping and the Ion Beam Figuring (IBF) technologies can be a very competitive solution for the realization of x-ray optics with excellent imaging capabilities and high throughput. While very thin mirrors segments can be realized by slumping with residual figure errors below few hundreds of nanometres, a non-contact and deterministic process (dependent on dwell time), like IBF, is a very effective post facto correction, as it avoids all the problems due to the handling and the supporting system. In the last years, the two processes were proven compatible with very thin sheet of Eagle XG glasses (0.4 mm thickness). Nevertheless, the fast convergence of the process is a key factor to limit the cost of the mirror plate production. A deeper characterization of removal function stability showed that its repeatability between each run has to be improved for a real enhancement of the process convergence factor. A new algorithm based on de-convolution has been implemented and tested, with important advantages in terms of calculation speed, minimum material removal and optimization possibilities. By analysing the metrological data of test slumped glasses, we showed how the IBF is effective in the correction of figure errors on scales above 8 - 10 mm. An overall figuring time of few hours is required with surface error around 100 nm rms. Thanks to the thickness measurement data, which are performed in transmission mode with an interferometric set-up, we demonstrated that it is possible to disentangle the effective amount of the material removed and the deformations introduced during the process.

Keywords: X-ray grazing-incidence telescopes, ion beam figuring, deterministic correction, X-ray segmented mirrors, hot slumping, Eagle glass

1. INTRODUCTION

The combination of a large effective area and of a high angular resolution is a powerful resource for the realization of a breakthrough x-ray mission. The reduction of the thickness of substrates enhances the geometric collecting area per unit of mass but, in general, increases the difficulties in realizing high quality mirrors. Moreover, production time and costs are additional factors concurring to the feasibility of a process.

In the framework of Lynx mission proposal [1], different techniques are being investigated for the mirrors production and assembly [2, 3, 4]. In the first case, large monolithic fused silica shells are realized with direct polishing technique, while in the second case, small segments of silicon are produced with direct polishing and then assembled in Meta-shells. In the third case, small segments of Eagle glass are hot-slumped and then equipped with piezoelectric actuators, adjustable to account for long-term stability and for in flight thermal distortion correction. The segments are then assembled into units.

---

[1] Corresponding author: marta.civitani@brera.inaf.it; www.brera.inaf.it
[2] Moved to Officina Stellare S.r.l., Italy
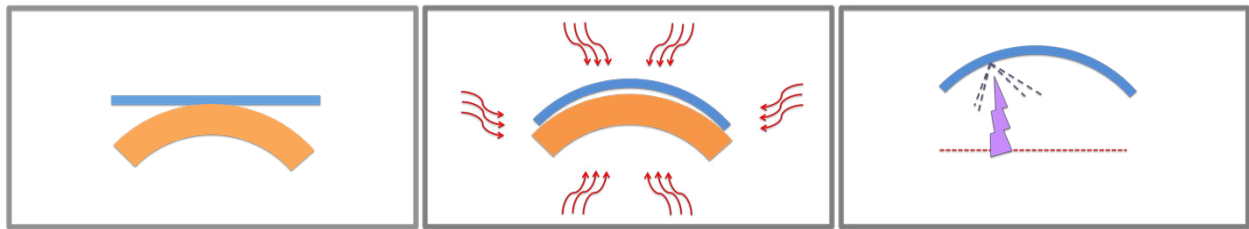
Figure 1-1: A simplified process for high angular resolution x-ray optics realization. The hot-slumping process (direct or indirect) of thin glass plates is followed directly by the ion beam figuring of the plates.

Given the size of the Lynx Mirror Assembly (LMA), the modular approach is competitive with respect to the others. The parallelization of the activities is straightforward: in dependence of the delivery time requirements, the number of productive lines can be defined. Therefore, we assume the mirror segment as the basic element. The segments are then assembled in X-ray Optical Units, which will compose the LMA. In order to keep the production of the mirror segments as simple as possible, we aim to investigate a two-steps approach. First, the glass segments are shaped to the desired figure by hot slumping, second, the residual figure error, if any, is corrected with Ion Beam Figuring (IBF). A simplified scheme of the process is shown in figure 1-1.

The hot slumping is a replica process with several advantages: it is cheap and high reproducible results are expected once the process is well established. The best results achieved so far are mirrors compatible with errors of the order of hundreds of nanometres, making a post facto correction indispensable for further improvement of their optical quality.

Given the small amount of material to be removed a deterministic technique is necessary. The choice of IBF is mainly driven by the required thickness of the substrates. A non-contact figuring technique represents a great simplification for the process set-up. There is no need of ad-hoc supporting system and all the problematic related to its print-through in the figuring results are avoided. The feasibility of this kind of process on very thin glasses (0.4 mm thick) was demonstrated in the last years. The results achieved on samples of Eagle glass were very encouraging:

- The micro-roughness of the figured surface remains compatible with x-rays requirements [5].
- The IBF does not introduce large unpredictable deformations in the substrate [6].

The demonstration of these two conditions was indispensable to assume the IBF as the last step of the substrates production process. In order to proof that the IBF is a viable solution with respect to the figuring time and to the results, a refinement of our IBF process was carried out.

The amount and the shape of material removed in the unit time, called removal function, is influenced by many parameters. The main parameters are the source settings, the material being processed and its surface quality. The knowledge of the removal function is necessary for determining the local figuring time: for each position of the surface map a corresponding amount of time needed for the correction is calculated. For a given surface error map, the corresponding map of the figuring time is called time matrix. The removal function characterization and the algorithm for the time matrix calculation are the main ingredients for the refinement of the process: the convergence factor of the figuring is fundamental to reduce the number of IBF runs and therefore the overall figuring time.

In this paper we present the progress in the IBF process characterization. The measurement configuration is summarized in paragraph 2. The removal function characterization is reported in paragraph 3-1 while the details of the new algorithm calculation are given in paragraph 3-2. The results achieved after the implementation of the new algorithm on a curved sample are presented in paragraph 4. The conclusions are summarized in paragraph 5.

2. MEASUREMENT CONFIGURATION

Two main measurement set-ups are used to evaluate the ion beam convergence capabilities. They are both based on interferometry. In one case, we looked at the figure error of the sample optical surface, while in the other case we measured its thickness variations in transmission mode.

The first interferometric set-up is available at Smithsonian Astrophysical Observatory (SAO). It is based on a 4D Technology FizCam 3000 interferometer equipped with a Computer-Generated Hologram (CGH) to adapt the wave front

to the cylindrical shape of the glasses. In order to prevent the problems caused by the reflection of the back surface, a thin layer of gold (40 nm thick) is deposited on the optical surface of the glass. A supporting system for the glass with two points on the bottom and one on the top is used to hold the glass sample during the measurement (see figure 2-1A). The accuracy of this metrological set-up is better than 30 nm rms [7].

The thickness measurements were performed at INAF-Brera Astronomical Observatory. We used a Zygo interferometer to generate a collimated beam 100 mm in diameter and a fused silica flat reference to close the optical cavity. This reference has the same size of the laser beam and has an optical quality of 84 nm RMS, almost due to a power error. In figure 2-1B a top view of the measurement set-up is shown.
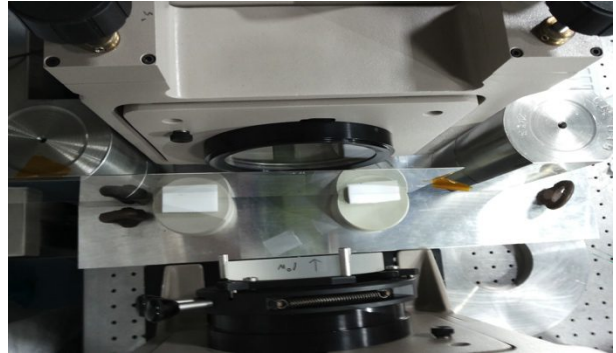
Figure 2-1: (A) The measurement set-up for the glass plate figure errors available at SAO. The interferometer beam is adapted to the cylindrical geometry with a CGH system. The glass plate is supported on two points on the bottom and one on the top back. (B) The thickness measurements set-up. A Zygo interferometer generates a collimated beam (100 mm in diameter). A fused silica flat reference closes the optical cavity in which is placed the thin glass sample.

3.   IBF PROCESS IMPROVEMENTS

In order to improve the convergence factor of our IBF facility and the expected performances, the main steps of the process (e.g. the removal function and the time matrix determination) were analysed. The following paragraphs report the results relevant to the removal function characterization and to the introduction of a new algorithm for the time matrix determination.

3.1 Removal function characterization

The Removal Function (RF) on thin glasses was determined in transmission mode by means of thickness measurements. This procedure has some advantages with respect to the standard approach to characterize the removal rate of the ion beam source: a flat reference surface, of the same material under study, is procured and is figured in fixed position for some minutes to get a measurable amount of material. As the removal rate can be function of the final substrate surface finishing quality, the procurement of these samples can be difficult in a development phases of a process. Moreover, due to the cost of the samples, the characterization of the removal function properties is in general limited to the minimum. For these reasons, the use of cheap thin substrates with the same surface quality to characterize the removal function introduces a great flexibility in the process verification and control:

- The RF can be repeated as many time as necessary. Its repeatability can be checked with respect to different ion beam runs, while within the same run we can infer its scalability with time and its stability.
- Witness samples, with the same surface quality of the mirrors, can be added to each figuring run for a better understanding of the process, both with respect to the removal rate properties and both with respect to the back sputtering phenomena characterization. They could be placed in different positions to evidence the back sputtering material arrival or the effectiveness of a masking system.

In general, the samples are not flat and high frequency thickness variations can disturb the computation of the removal function properties. We recommend a quick check of the glass samples, which is easy and fast under sodium lamp.
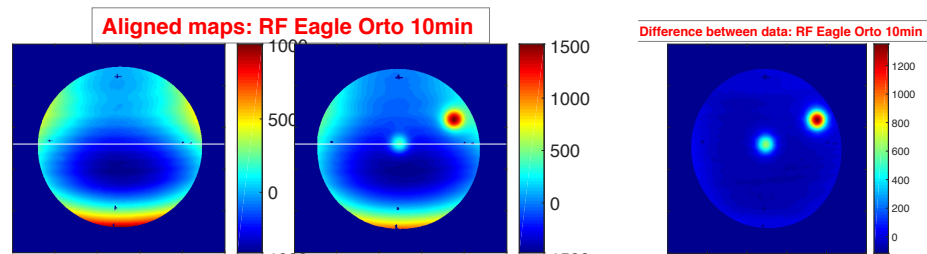
Figure 3-1: Removal Function as acquired on the Eagles glass. (A) Thickness variation on a glass area. (B) Thickness variation as acquired after the RF has been figured. In the displayed case two RF are visible in the measured area. (C) Differences between the initial and the final maps, highlighting the two peaks of different amplitudes due to the different settings.

The process to measure the RF is shown in figure 3-1 with an example. The initial thickness measurement of the glass is shown on the left side. The central panel reports the same measurement repeated after the figuring of two RFs. The RFs print-through is obtained subtracting the two maps (with the correct alignment). The result is reported in the panel on the right. In order to derive the size and amplitude parameters needed for a first evaluation of the performances, the shape of the ion beam RFs are fitted with 2D Gaussians. The used function is $G(x,y) = A1* \exp ((x-x_0)^2/\sigma_x + (y-y_0)^2/\sigma_y)$. A1 is the linear coefficient and is related to the removal rate while σ_x and σ_y are related to the width of RF in the two orthogonal directions and account for the RF symmetry.
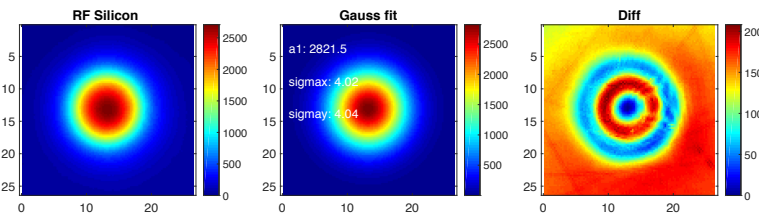

Figure 3-2: Measured (A) and 2D Gaussian fit (B) of the RF data acquired on a silicon sample. (C) The difference between the two. In all the images, the colour scale is in nanometres.

An example of the data, derived from a standard thick flat substrate, is shown in figure 3-2 The real RF and its 2D Gaussian fit are overlapped in the left panel. The difference is shown in the right panel. In this case, the peak of the measured RF appears shallower than the best-fit Gaussian. The Peak To Valley (PtV) of the map difference is 8% of the original RF map. From a general point of view, the data of the RF on silicon (named case#4 in table 1) presents higher removal rate and shallower shape.

The data acquired on thin Eagle glasses are summarized in table 1. They have been collected during the time and in different ion beam figuring test campaigns. In order to have a clear understanding of the RF properties, the dependence from the distance and from the incidence angle has been explored. Moreover, the repeatability of the RF in terms of removal rate and shape was evaluated within and outside the same IBF run.

First data on thin glass samples were acquired in 2016 at a working distance of 36 mm from the surface. The RF was repeated in the same run for different durations (10 min, 20 min and 30 min) in different positions to characterize the final micro-roughness on the surface in dependence of the amount of material removed. With respect to the removal rate scalability with time, the data reported in the table show that the average removal rate on the period of the order of 10 - 30 min is quite good as the results scales within 20 nm error in amplitude. There is a systematic difference of less than 5% in the width of the RF along the two axes. This feature is judged due to the asymmetric waviness in the surrounding area of the RF.

In general, when dealing with substrates for x-ray optics, the samples have pseudo conical geometries. Therefore, depending on the radius of curvature, the incidence beam direction can play a role in the system performances, being the removal rate higher on not-normal surfaces. To account for this effect, a corrective factor should be applied in the figuring and a specific test was carried out to measure it. Two new samples were positioned in the vacuum chamber. One of the samples was orthogonal to the ion beam source and was used to check the repeatability within different runs of the

system. The other sample was aligned with 13° with respect to the incident beam. This misalignment angle was chosen in accordance with the maximum slope expected on the cylindrical sample we are dealing with. The set-up of the experiment is shown in figure 3-3. The distance of the samples was higher than in the past and most compliant with the ion beam source requirements. Two RF were figured for each of the samples considering 10 min and 20 min integration time. The removal rate with the sample misaligned of 13° is higher by 16%. The FWHM is a little larger but with no specific correlation with the direction of the tilt, which was along x direction (Case#8 and Case#9 of table 1). Therefore, if no corrective factor is implemented, the final expected effect on the figuring accuracy is decreasing around 1% for each degree of tilt. The RFs, determined in the orthogonal and in the misaligned direction, are shown in figure 3-4 the (left and right panels). The RF figured by doubling the integration time is reported in the bottom parts of the figure. For each of the cases, the raw data, the 2D Gaussian fit and the residua with respect to the fit are shown. The residual errors with respect to the fit are in all these cases opposite in sign with respect to the one observed on the silicon (taken at the same working distance). The RFs are sharper in the central part and this is can be an advantage in the correction of higher frequency errors on the surface.
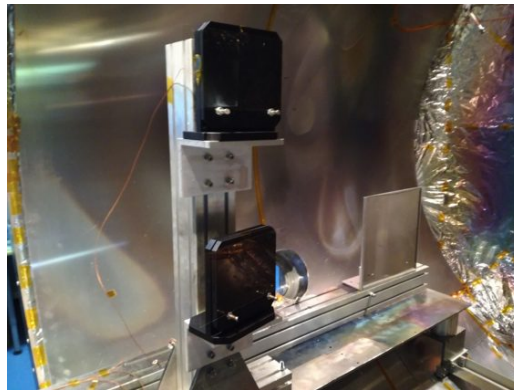

Figure 3-3: Set-up for the test on the RF dependence from the incidence angle of the ion beam. The flat glass sample on the top is orthogonal to the beam, while the flat sample on the bottom is oriented with an angle of 13° with respect to the beam direction.
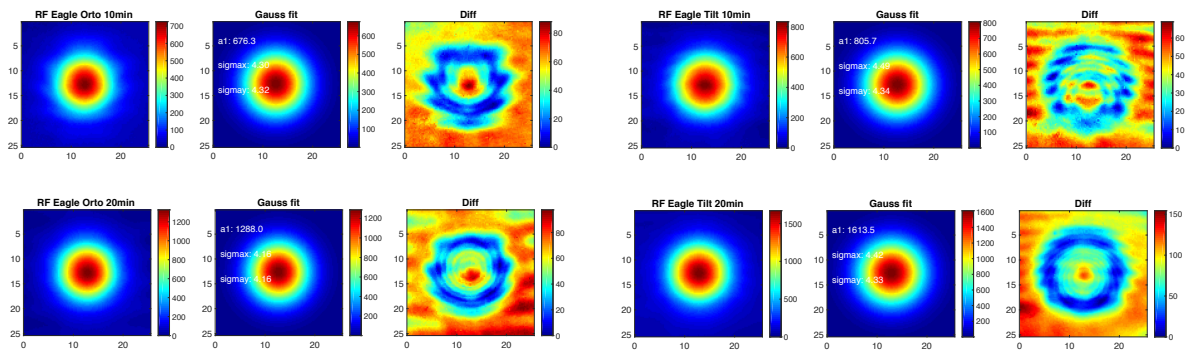

Figure 3-4: Determination of the RF dependence from the incidence angle of the ion beam. On the left, the RF acquired in orthogonal direction, while on the right the RF acquired with the target surface misaligned by 13°. For both the cases the RF has been repeated twice, doubling the integration time to check for linearity (top and bottom). Each of the measured RF is displayed together with its Gaussian fit and with the difference with respect to the fit.

We observed that the removal rate and the lateral width depend on the distance of the surface. The data for Case#1-2-3 were acquired at 36 mm distance while the data for Case#4-5-6 at 60 mm. When the source is nearer to the substrate the removal rate is higher of about 14%. Left side of Figure 3-5 reports the residua with respect to the fit of the RFs at 36 mm distance with an integration time of 10-20-30 min. The RF peaks result sharper with respect to Gaussian with lower FWHM. In general, the source movements follow the sample geometry in terms of distance to avoid this kind of inaccuracy.
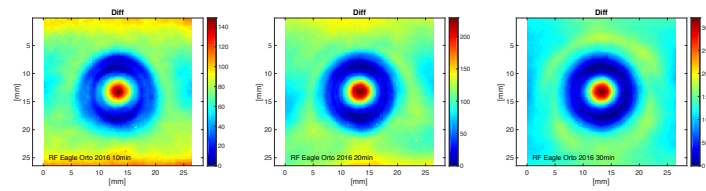
Figure 3-5: Differences with respect to the Gaussian best fit for RF acquired at 36 mm distance with integration time of 10, 20 and 30 min. Colour scale is in nanometres.

The removal rate is not fully scalable if the integration time is divided in parts. The Case#6 RF was generated dividing the integration time in two parts (17 min + 3 min). Case#7 RF refers to a continuous 20 min long figuring. This indicates that the stability of the source on the short term can be a problem.

The last two test cases reported in table 1 were dedicated to a final check for repeatability of the RF over different runs. Two similar setting were verified. S5 corresponds to the one used so far while S3 slightly differs from S5 (Beam Voltage is equal to 750 V instead of 1000 V, while Beam Current is 5 mA in both cases). The removal rates (Case#10 and Case#11) are different from the previous results and shows that the characterization of the RF outside of the run introduces an error of the order of 6%. Moreover also the shape of the RF is different, as reported in figure 3-6 for the two cases. These results show that the average stability of the source is good on time scale up to 30 min. Instead the repeatability of the source setting across different ion beam runs is poor. This problem can be solved with the introduction of a Faraday cup.
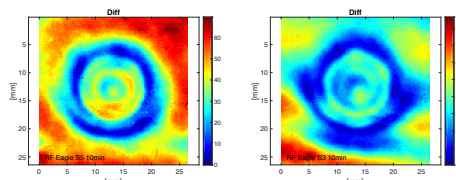

Figure 3-6: Differences with respect to the Gaussian best fit for RF acquired at 60 mm distance with integration time of 10 minutes with S5 and S3 settings. Colour scale is in nanometres.

Table 1: Main RF parameters as derived from 2D Gaussian fit on data acquired in the last two years on thin glasses.

		Settings	Dist. (mm)	Time (min)	A1 (nm)	Sigmax (nm)	Sigmay (nm)
	2016	--	--	--	--	--	--
1	Orto	S5	36	10	782.7	3.72	3.91
2		S5	36	20	1561.4	3.73	3.83
3		S5	36	30	2357.2	3.73	3.79
	2017	--	--	--	--	--	--
4	Orto(Silicon)	S5	60	17	2882.3	4.03	4.04
5	Orto	S5	60	10	676.3	4.30	4.32
6	Orto (restarted)	S5	60	20	1288.0	4.16	4.16
7	OrtoBis	S5	60	20	1356.6	4.62	4.21
8	Tilt	S5	60	10	805.7	4.49	4.34
9	Tilt	S5	60	20	1613.5	4.42	4.33
10	Orto	S3	60	10	702.2	4.86	4.91
11	Orto	S5	60	10	716.0	4.62	4.43

From a general point of view, the RF depends on the distance and the orientation of the surface both with respect to the removal rate and to the removed pattern. These effects should be properly taken into account in order to increase the convergence rate of the process. In order to avoid problems with the features introduced with the thickness variation the usage of radially symmetric fit functions is recommended.

3.2 Time matrix algorithm optimization

The correction of the figure error with IBF is based on dwell time: the ion beam source is moved in front of the surfaces (X axis and Y axis), at constant distance from the target (with an additional Z axis), removing at each position an amount of material proportional to the time spent in that position. The amount of time that the ion source has to stay in each of the surface positions depends on the amount of the error in that particular position and in the neighbouring area. In fact, the removal of material is extended to the footprint of the RF. For an accurate correction, the amount of material removed from the entire RF should be taken into account. The solution to this problem is what we call 'time matrix' determination: a value of figuring time is determined for each of the positions of the surface. The implementation of the correction can be realized 'point by point', driving the carriage to keep the source for the defined amount of time in the defined positions. As an alternative, the carriage velocity can be modulated so that the source will spend on a given area the desired time.

The current algorithm for the time matrix calculation is based on an iterative process. [7,8] At each interaction the entire surface is taken into account and the dwell time corresponding to the remaining error added. The run time of the algorithm is quite long and could last hours. Moreover, depending on the initial features to be corrected, the convergence of the process can result in dotted time matrix, which could lead to an orange peel correction. An example of a dotted-like time matrix is reported in figure 3-7, where the possible correction to be applied to a cylindrical test sample is shown. Note that an additional frame of data is added to the real area in order to take into account correction of the edges. The 'orange peel' effect depends on the initial figure error map amplitude and distribution, but it is clearly undesired in x-ray optics, where the waviness on the millimetre scale has to be avoided. The dotted like maps can be post-processed with a smoothing, but an algorithm, which converges directly to the best solution, is much more effective and desirable.
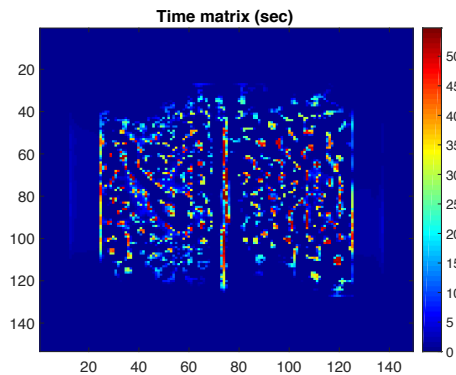

Figure 3-7: Time matrix as calculated by the current IBF algorithm.

Therefore a new quick algorithm to calculate the time matrix based on the de-convolution of the removal function has been prepared. The amount of material removed is represented by equation (1). The beam function B returns the depth of the material removed per unit of time, while the time matrix function T is the time spent in a given location per unit of area.

$$R(x,y) = \sum_i \sum_j B\big(x - u_i, y - v_j\big) * T\big(u_i, v_j\big) * \Delta_u * \Delta_v \quad (1)$$

Given the amount of material to be removed R(x,y) and the beam function B(x,y), the time matrix can be derived trough de-convolution. The algorithm is based on Fast Fourier Transform and runs very fast (less than 0.1 sec). It offers the best mathematical solution. Moreover it allows an easy and fast comparison of the results in different conditions (e.g. different removal functions).

The edges' figuring is taken into account with the introduction of an additional frame of simulated data. The width of the frame is defined in relation of the RF size. The frame is filled interpolating the errors measured on the edges of the sample down to the edge of the frame. In order to reduce to the minimum the figuring time for this additional area, the simulated error on the external edge is set to zero. The area to be effectively figured can be smaller than the one used for the calculation. In general, the greater is the frame, the greater will be the figuring duration. The minimum frame size can be determined in accordance with the requirement on the surface edges.

In general, a first simple optimization of the results can be selected in systematic way defining the maximum time per pixel on the time matrix: the correction of particular feature, like localized bump, can be avoided setting an upper limit to the maximum time per pixel. As well, the correction of deeper regions can be avoided subtracting the corresponding maximum working time from the overall map.

An example of the algorithm results is shown in figure 3-8. The initial residual map, the extended data, the RF, the time matrix, the expected removed material and final residua in the initial area are shown. In order to highlight the IBF capabilities with respect to the RF shape, the initial map has been generated rescaling data from an old test slumped glass sample which was characterized by high frequency figure errors. The initial rms of the surface is 227 nm and is shown in the 'Init' panel. A trial extended map with a frame is shown in 'ToDo' panel. The RF is reported in the third panel. A Gaussian shape with a FWHM of 8 mm and a maximum removal rate of 1.3 nm/sec at the peak was selected. The time matrix is shown on the bottom. The overall figuring time is 16.55 hours, pretty similar to the one calculated with standard algorithm (15.4 hours). Thanks to the de-convolution algorithm, it is smoother and no orange peel effect is expected on the surface. This is a great advantage with respect to the process. The implementation of the time matrix in terms of carriages velocity modulation is straightforward and does not need any additional post-processing. The expected removed material is reported in 'ToBeRemoved' panel, while the expected residua on the surfaces is shown in the 'residual error' panel. Due to the particular error distribution of the surface, the high frequency pattern remains.

As suggested before, the optimization of the overall figuring time can be pursued adjusting the limits on the errors on the map. In particular a limit in the depth of the holes to be accounted for reduce significantly the amount of material to be removed. Instead, the high frequency pattern correction can be operated only focusing the beam. In figure 3-9 and 3-10 the results achievable with Gaussian RF respectively 6 mm FWHM and 4 mm FWHM are shown. As expected, the assumption of the same removal rate increases the total figuring time by a factor 4. On the other side, the residual high-frequency error is reduced by a factor two, passing from 78.5 nm to 39.7 nm rms. The colour scale of the residual maps is set to [-100, 100] nm in all the figures.

The high frequency content of the residual map depends on the initial error map. In figure 3-11 is shown the expected IBF result for a slumped glass sample with a higher peak to valley error, but lower content of high frequencies errors. In this case the process is expected to converge directly to 34.5 nm rms with a limited amount of high frequencies. In this case there is no need of any focalized beam to correct of the sample errors.
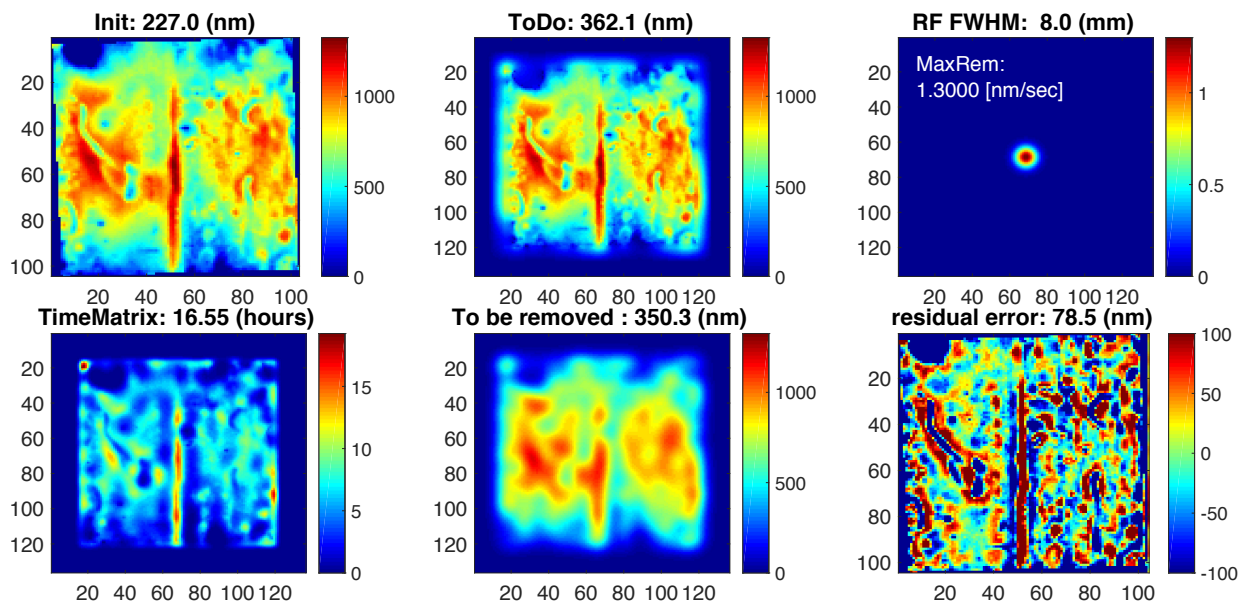
Figure 3-8: De-convolution algorithm applied on a figure error map with a high frequency error (S03). From left to right and then from top to bottom: the initial residual map, the extended data with the simulated frame, the RF used for the calculation, the derived time matrix, the expected removed material (resulting from the convolution of the time matrix and the removal function) and the final residua on the real portion of the surface.
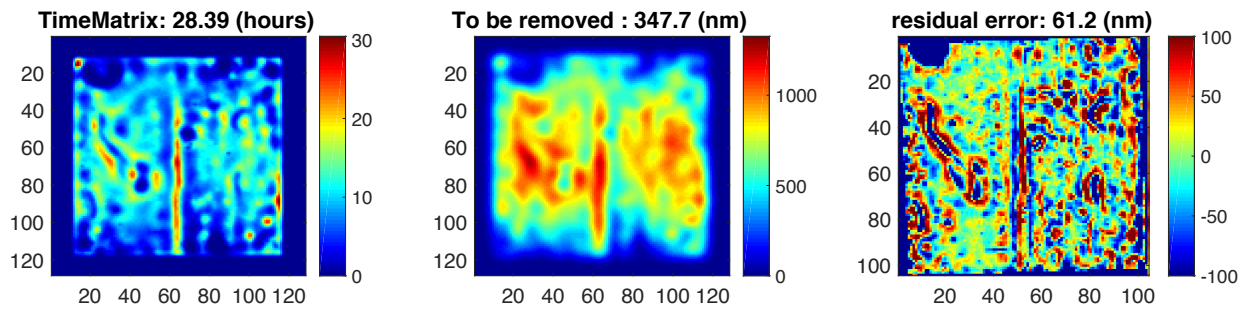
Figure 3-9: The time matrix correspondent to the same input error of figure 3-8 is calculated with a Gaussian RF with 6 mm FWHM and the same removal rate at the peak. (A) Time matrix. (B) Theoretical removed material. (C) Uncorregible final error.

Figure 3-10: The time matrix correspondent to the same input error of figure 3-8 is calculated with a Gaussian RF with 4 mm FWHM and the same removal rate at the peak. (A) Time matrix. (B) Theoretical removed material. (C) Uncorregible final error.
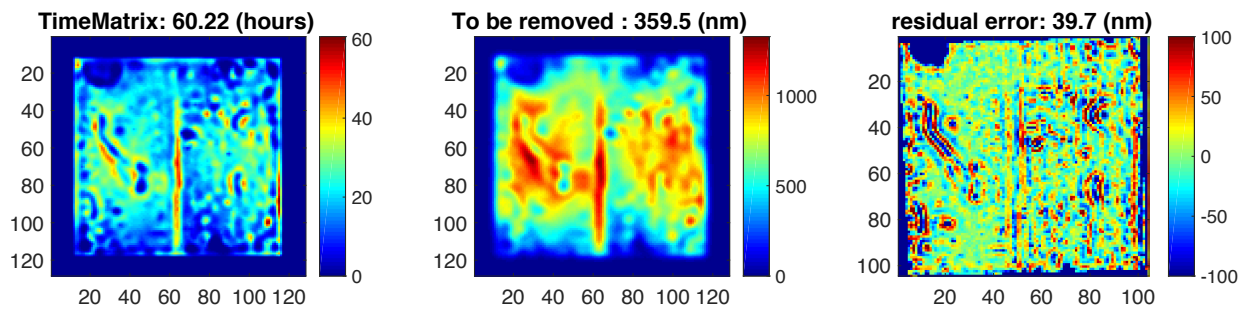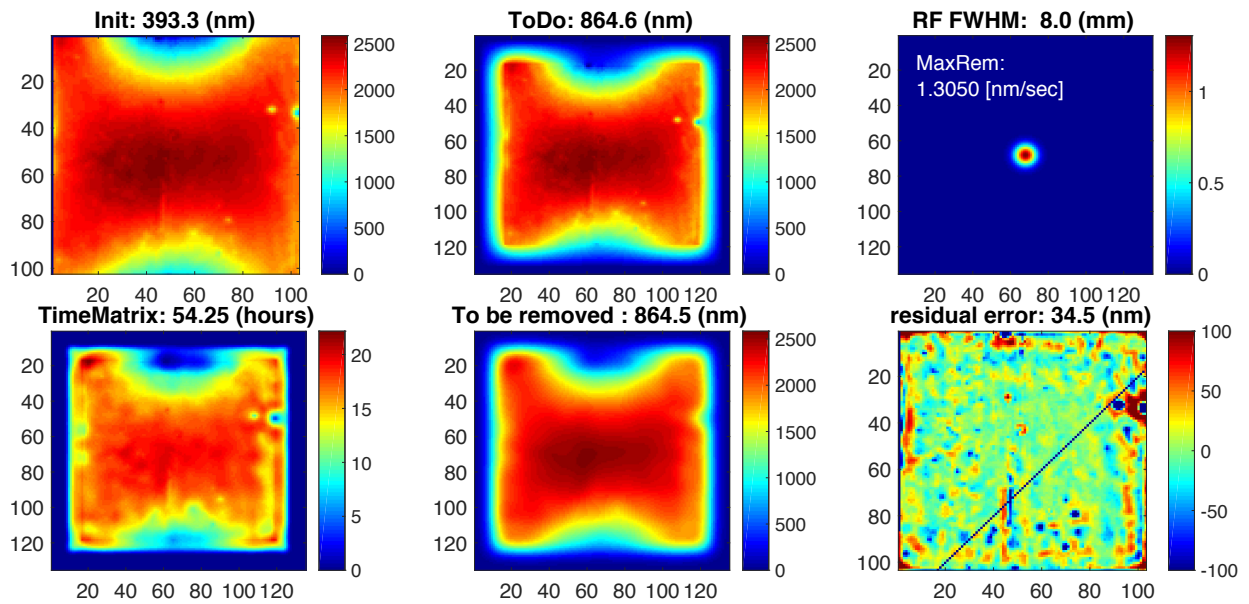

Figure 3-11: Simulated correction based on error map of slumped glass sample S05, assuming a Gaussian RF (A1 =783nm/sec, FWHM = 8 mm)
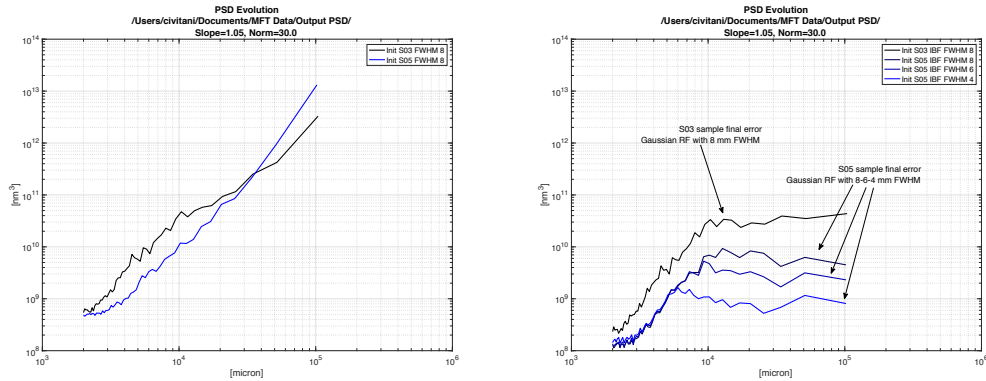
Figure 3-12: Power Spectral Density of the initial (left) and final (right) figure error map expected for the cases considered.

The improvement in terms of frequency domain is better clarified calculating the Power Spectral Density (PSD) of the initial and the final expected data. The results are shown in figure 3-12. The left figure reports the average PSD as derived from the input error maps. In one case the low frequency error was lower but higher frequency errors characterized the map (S03). In the other case, the input map was dominated by low frequency errors. The right figure shows the average PSD expected on the residua. For all the cases, there is a flattening of the PSD for scales larger than 5, 7 and 9 mm. This reflects the RF width used in the calculation. The smoothing at higher frequency does not change the PSD slope but just decrease the amplitude of the features, independently from the RF width.

From a general point of view, the time matrix reported as examples correspond to quite large overall figuring time. The results can be scaled down linearly for higher removal rate or, on the contrary, smaller input errors. For the beam function, which gives 1.3 nm/sec removal rate at the peak, errors of around few hundreds of nm peak to valley can be corrected with IBF runs of some hours.

4. TEST RESULTS

In order to test the new algorithm and to verify if the knowledge acquired on the RF was effective in the improvement of the convergence factor of the IBF process, a preliminary test was carried out. We chose to work on a test sample in cylindrical configuration, realized with direct hot slumping [9]. Given that the aim of this test was the debugging of the new set-up, no specific requirements were posed on the initial figure error, on the contrary a lower quality surface was judged more probative.
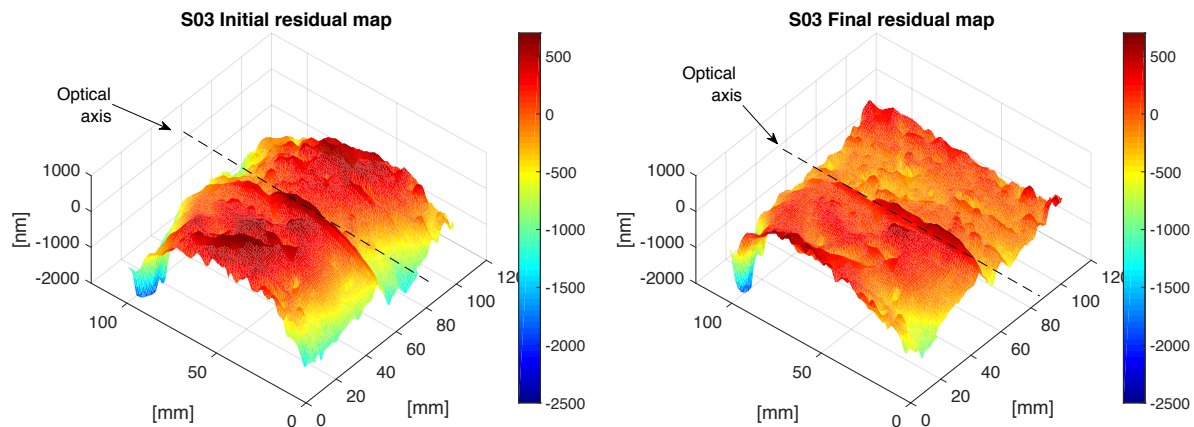

Figure 4-1: (A) The initial surface error of the sample under figuring (S03) with respect to the best fit cylinder with radius of curvature 222.3 mm. (B) The final surface error with respect to the best fit cylinder.

The sample S03, slumped on a poor quality mould, was considered a good test opportunity. Its initial figure error is shown in figure 4-1a: the initial low frequency error is around 2 microns PtV and the higher frequency pattern can be used to check for the alignment and figuring accuracy. In order to generate a corrective map compatible with few hours figuring time, the low frequency part of the initial error was scaled down so that the input error map for the algorithm was reduced to 220 nm rms.

The comparison between the thickness variation maps acquired in transmission mode before and after the IBF returns the amount of material removed from the sample. See figure 4-2a. The spread between the material removed and the expected removal returns the accuracy of the process. The achieved results are shown in figure 4-2b. The input map is displayed as a continuous surface while the measured amount of material removed is now traced with contour level. In order to avoid an additional factor of uncertainty coming from the surface reconstruction with patches, only the data corresponding to the interferometer aperture (100 mm diameter) are reported: in this region, the figuring accuracy error is 35.8 nm rms, improving by a factor 2 the results achieved in a previous test [6].
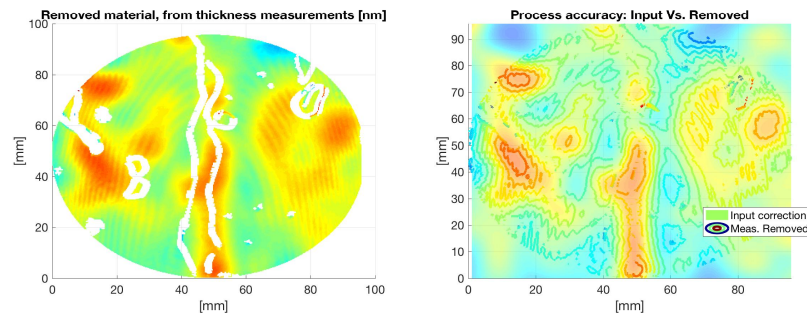

Figure 4-2: (A) Removed material, as derived from the thickness variation maps. Marker traces, which were present on the back surface of the glass, are shown in white. (B) The input map is displayed as a continuous surface, while the measured amount of material removed (figure 4-2a map) is now traced with contour level.
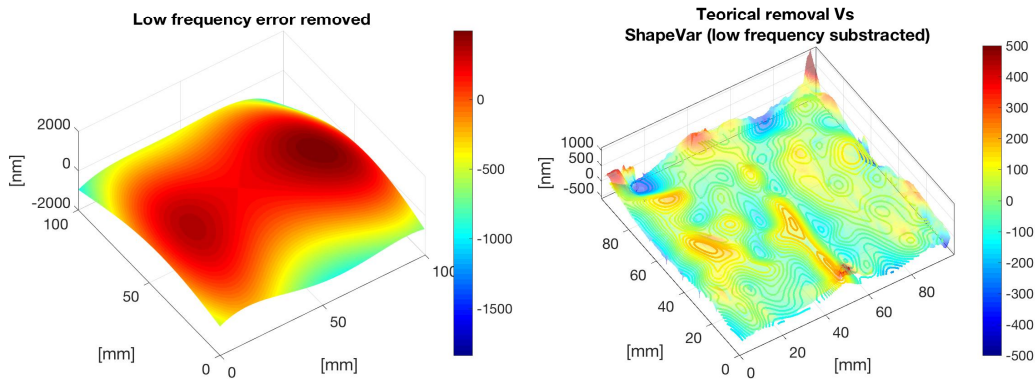

Figure 4-3: (A) The low frequency error on the sample derived with 2D polynomial fit of the residual data. (B) The remaining higher frequency error after the polynomial fit.

The measured shape error after the figuring is reported in figure 4-1b. The surface is clearly flatter along the optical axis, even if no major correction was operated to this aim. On the other side, the higher frequency pattern variation is pretty similar to the input one (reported in figure 4-2b, continuous surface data set). In order to highlight the situation, the measured difference in shape can be divided into two components. The low frequency error is reported in figure 4-3a in polynomial form. Its overall shape is very similar, in amplitude and in shape to the one that characterize the initial shape error of the glass. At the same time, the high frequency error is well in line with the input map. In figure 4-3b the surface corresponding to the commanded removal is shown with contour plot, while the shape variation (after the subtraction of the low frequency error) is semi-transparent. The shape variation measurements confirm that the correction is effective for higher frequency errors. Instead, the low frequency variation was not expected, as it was not accounted in the

commanded removal. Moreover, such a variation was not observed in the test performed in the past [6] on cylindrical slumped glass. Nevertheless, it is a quite interesting effect, as it significantly reduces the deformation on the sample on the larger scale. If this dumping effect were due to stress release on the sample, it could greatly improve the speed of the process, reducing a lot the amount of material to be removed to get the correct sample figure. At the present stage, we do not have additional data on the repeatability of this dumping effect, neither on its predictability in terms of the initial shape or slumping process parameters. These are fundamental aspects to be accounted for a positive usage of this effect. Further tests will be carried out in the future to explore this possibility.

On the other hand, if this dumping effect will turn out not predictable or repeatable, being just a not controlled deformation in the sample due to the thermal loads, there are still some margins for its mitigation. In the current set-up, the glass sample was simply supported on two points on the bottom and on one point on the top. No particular tricks were introduced for the thermal load reduction. Additional conductive structures may be placed on the back of the sample to distribute and to disperse faster the heat.

In the end, the outcome of the test is very positive, as it showed an improvement of a factor 2 in the figuring process accuracy. Furthermore, it demonstrates the possibility to disentangle the effective removal from the substrate deformations. The thickness measurements return the amount of removed material, while the interferometric measurement of the surface report the shape variation. Moreover, a possibility for the reduction of the figuring time emerged, as part of the initial post-slumping figure error was cancelled for free. This would be a great opportunity enhancing the sustainability of the process with respect to the time and to the costs. A complete and systematic characterization will be carried out to assess the repeatability and the effectiveness of this effect on different samples.

5. CONCLUSIONS

The combination of a large effective area and of a high angular resolution is a powerful resource for the realization of a breakthrough x-ray telescope. In order to increase the geometric collecting area per unit of mass, the thickness of substrates should be limited. A possible solution is based on a modular concept with very thin mirrors made of glass, assembled into Optical Unit. In general, the limited thickness of the segments increases the difficulties in achieving good optical performances. We investigate a possible realization process based on two steps: first, the glass substrates are shaped with hot slumping and then they are figured with IBF to correct the residual slumping errors. The hot slumping is a based on the replica approach and therefore well adapted to the scale production. On the other hand, the ion beam figuring is a high deterministic technique and being a contactless technique, it offers indubitable advantages in the case of very thin substrates.

In the last years, preliminary tests on slumped samples were carried out with promising results. Nevertheless, the fast convergence of the process is a key factor to limit the cost of the mirror plate production. A deeper characterization of removal function stability showed that its repeatability between each run has to be enhanced for a real improvement of the process convergence factor. A new algorithm based on de-convolution has been implemented and tested, with important advantages in terms of calculation speed, minimum material removal and optimization possibilities. In particular it accounts for the smoothing of the dotted pattern in the time matrix: this is a major improvement for the x-ray optics as it helps it prevents the mid-frequency generation. Analysing the metrological data of test slumped glass we showed how the IBF can be effective in the correction of figure errors above 8 - 10 mm. Values of rms compatible with few hours figuring are around 100 nm.

Thanks to the thickness measurement data, which are performed with an interferometric set-up and return the amount of material removed, we were able to clear disentangle the effective correction and the deformations introduced by the process. In the performed test, the absolute error in the correction was of 35 nm rms, improving of a factor 2 the previous test results [6]. Moreover, we observed that, for the slumped glass under test, the main part of low frequency error has been cancelled for free. At the present stage, we do not have data to assess the repeatability and the effectiveness of this dumping effect for different samples. This feature will be certainly considered in the future tests, as it represents a great opportunity for the reduction of the figuring time, enhancing the sustainability of the process with respect to the time and to the costs.

6. REFERENCES

(1) Jessica A. Gaskin, Ryan Allured, Simon R. Bandler, Stefano Basso, Marshall W. Bautz, Michael F. Baysinger, Michael P. Biskach, Tyrone M. Boswell, Peter D. Capizzo, Kai-Wing Chan, Marta M. Civitani, Lester M. Cohen, Vincenzo Cotroneo, Jacqueline M. Davis, Casey T. DeRoo, Michael J. DiPirro, Alexandra Dominguez, Leo L. Fabisinski, Abraham D. Falcone, Enectali Figueroa-Feliciano, Jay C. Garcia, Karen E. Gelmis, Ralf K. Heilmann, Randall C. Hopkins, Thomas Jackson, Kiranmayee Kilaru, Ralph P. Kraft, Tianning Liu, Ryan S. McClelland, Randy L. McEntaffer, Kevin S. McCarley, John A. Mulqueen, Feryal Özel, Giovanni Pareschi, Paul B. Reid, Raul E. Riveros, Mitchell A. Rodriguez, Justin W. Rowe, Timo T. Saha, Mark L. Schattenburg, Andrew R. Schnell, Daniel A. Schwartz, Peter M. Solly, Robert M. Suggs, Steven G. Sutherlin, Douglas A. Swartz, Susan Trolier-McKinstry, James H. Tutt, Alexey Vikhlinin, Julian Walker, Wonsik Yoon, William W. Zhang, "Lynx Mission concept status", Proc. SPIE 10397, UV, X-Ray, and Gamma-Ray Space Instrumentation for Astronomy XX, 103970S (19 September 2017); doi: 10.1117/12.2273911; https://doi.org/10.1117/12.2273911

(2) Zhang, W.W., Allgood, K.D., Biskach, M.P., Chang, K.-W., Hlinka, M., Kearney, J.D., Mazzarella, J.R., McClelland, R.S., Numata, A., Olsen, L.G., Riveros, R.E., Saha, T.T., Solly, P.M., "Monocrystalline Silicon and the Meta-shell Approach to Building X-ray Astronomical Optics,", paper 10399–27 (2017)

(3) M. M. Civitani, J. Hołyszko, G. Vecchi, S. Basso, O. Citterio, M. Ghigo, G. Pareschi, G. Parodi, S. Incorvaia, "Thin fused silica shells for high-resolution and large collecting area x-ray telescopes (like Lynx/XRS)", Proc. SPIE 10399, Optics for EUV, X-Ray, and Gamma-Ray Astronomy VIII, 103990W (12 September 2017); doi: 10.1117/12.2275263; https://doi.org/10.1117/12.2275263

(4) Casey T. DeRoo, Ryan Allured, Vincenzo Cotroneo, Edward N. Hertz, Vanessa Marquez, Paul B. Reid, Eric D. Schwartz, Alexey A. Vikhlinin, Susan Trolier-McKinstry, Julian Walker, Thomas N. Jackson, Tianning Liu, Mohit Tendulkar, "Deterministic figure correction of piezoelectrically adjustable slumped glass optics," Journal of Astronomical Telescopes, Instruments, and Systems 4(1), 019004 (19 March 2018). https://doi.org/10.1117/1.JATIS.4.1.019004

(5) M. Civitani, M. Ghigo, J. Hołyszko, G. Vecchi, S. Basso, "Ion beam figuring of thin glass plates: achievements and perspectives", Proc. SPIE 9905, Space Telescopes and Instrumentation 2016: Ultraviolet to Gamma Ray, 990578 (19 July 2016); doi: 10.1117/12.2233821; https://doi.org/10.1117/12.2233821

(6) M. Civitani, M. Ghigo, J. Hołyszko, G. Vecchi, S. Basso, V. Cotroneo, C. T. DeRoo, E. D. Schwartz, P. B. Reid, "Advancements in ion beam figuring of very thin glass plates (Conference Presentation)", Proc. SPIE 10399, Optics for EUV, X-Ray, and Gamma-Ray Astronomy VIII, 103991E (21 September 2017); doi: 10.1117/12.2275555; https://doi.org/10.1117/12.2275555

(7) Mauro Ghigo, Oberto Citterio, Paolo Conconi, Ralf Loi, Francesco Mazzoleni, "Perspectives of ion beam polishing of mandrels for x-ray replication optics", Proc. SPIE 2515, X-Ray and Extreme Ultraviolet Optics, (20 June 1995); doi: 10.1117/12.212628; https://doi.org/10.1117/12.212628

(8) M. Ghigo, G. Vecchi, S. Basso, O. Citterio, M. Civitani, E. Mattaini, G. Pareschi, G. Sironi, "Ion figuring of large prototype mirror segments for the E-ELT", Proc. SPIE 9151, Advances in Optical and Mechanical Technologies for Telescopes and Instrumentation, 91510Q (28 July 2014); doi: 10.1117/12.2056769; https://doi.org/10.1117/12.2056769

(9) Vincenzo Cotroneo, Ryan Allured, Casey T. DeRoo, Kenneth L. Gurski, Vanessa Marquez, Paul B. Reid, Eric D. Schwartz, "Thermal forming of glass substrates for adjustable optics (Conference Presentation)", Proc. SPIE 10399, Optics for EUV, X-Ray, and Gamma-Ray Astronomy VIII, 103990Y (5 October 2017); doi: 10.1117/12.2275738; https://doi.org/10.1117/12.2275738